Technical Article

(Semi-) analytical models for the design of high-precision permanent magnet actuators

***Abstract* — This paper discusses (semi-) analytical modeling techniques which are applied in the analysis and design of high-precision actuators which contain large multi-dimensional magnet arrays. Such high-precision actuators are being designed for application in the lithographic industry. The methods presented in this paper offer not only a significant reduction of the calculation time compared to three-dimensional finite element simulations, but also allow the calculation of force distributions inside the permanent magnet structures. The application of these models for the design of magnetically levitated planar actuators and for gravity compensation is discussed in detail.**

I. Introduction

Actuators which are applied in high-precision equipment have to combine both a high force density and good predictability of this force. The high force density is needed to achieve sufficient acceleration and speed levels, and to gain an adequate throughput of products, whereas a very good predictability of the force is required to obtain the necessary accuracy. Examples of such actuators are electromagnetic vibration isolators (gravity compensators) and magnetically levitated planar actuators.

Usually, these actuators have three-dimensional designs and lack periodicity or symmetries due to the integrated active magnetic bearings. The use of three-dimensional finite element methods is unpractical for the design of these actuators because electromagnetic quantities have to be calculated with a high spatial resolution and many design evaluations are required, which results in extreme calculation times. Moreover, for the calculation of force distributions inside magnet arrays, finite element methods are currently not suitable. Therefore, analytical and semi-analytical electromagnetic models and design tools are indispensable in the analysis and design of high-precision electromagnetic actuators.

In this paper, an overview of the semi-analytical techniques used to calculate the force, torque and force distributions in high-precision electromagnetic actuators will be given, with a focus to electromagnetic vibration isolators and magnetically levitated planar actuators. In sections II and III both applications will be introduced. The magnet models based on surface charges are discussed in section IV. Force calculation methods between magnets and their application for the design of electromagnetic vibration isolation are explained in section V. In section VI the forces and torques between magnets and coils are presented. Harmonic models based on Fourier series, which can be very effectively used for the analysis and design of planar actuators, are discussed in section VII. With these models the force and torque ripples of commutated planar actuators can be predicted and these are shown in section VIII. The conclusions are given in section IX.

II Magnetically levitated planar actuators

Positioning systems in high-precision machines often consist of stacked linear drives which are supported by air-bearings. To reduce the moving mass and to make the system vacuum compatible, magnetically levitated planar actuators are being investigated as alternatives to these stacked drives. The planar actuators have one moving member, which is suspended above the stator with no support other than magnetic fields. The gravitational force is fully counteracted by the electromagnetic force. The translator of these ironless planar actuators can move over relatively large distances in the *xy*-plane (2D-plane) only but it has to be controlled in six degrees-of-freedom because of the active magnetic bearing.

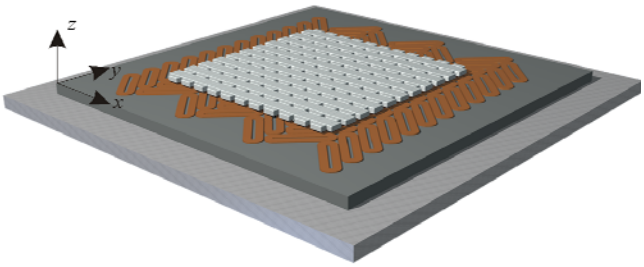

Fig. 1. Magnetically levitated moving-magnet planar actuator.

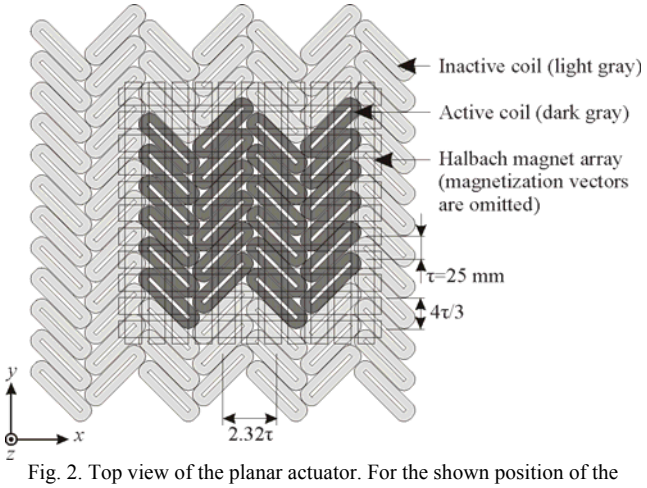

Fig. 2. Top view of the planar actuator. For the shown position of the magnet array, the dark coils are active.

Planar actuators can be constructed in two ways. The actuator has either moving magnets and stationary coils [1,2,3,4,5,6] or moving coils and stationary magnets [7]. The first type of planar actuator does not require cables for electrical and mechanical (cooling) connections to the moving part. In [5], a 6-DOF, long-stroke, moving-magnet, planar actuator is investigated and realized. Fig. 1 shows an overview of the actuator. The stator of this actuator consists of 84 coils of which only 24 are simultaneously energized. The moving part is a carrier with a permanent magnet array having a quasi-Halbach magnetization. During the movements in the *xy*-plane, the set of active coils changes with the position of the translator, because only the coils below and near the edge of the magnet array can produce significant force and torque. As a result, the 2D-stroke of this planar actuator is only limited by the size of the array of stator coils, and can be made, theoretically, infinitely large. Fig. 2 shows a top view of the actuator. The active set of 24 coils is indicated in dark gray for the shown position of the magnet array.

Although the actuator can be classified as an AC synchronous motor, DQ0- decomposition cannot be used for the decoupling of flux and current and consequently of force, torque and current. Therefore, new decoupling and commutation methods have been developed and every coil is excited with a single-phase current amplifier. It needs emphasizing that the current waveforms are non-sinusoidal [8].

III Electromagnetic Vibration Isolators

In many applications a platform needs to be resiliently isolated from vibrations. This system should simultaneously exhibit high stiffness with respect to force or torque exerted on the body itself and low stiffness with respect to vibrations caused by unforeseen disturbances from the environment. In high-performance suspension systems active elements are introduced, often being hydraulic, pneumatic or electromagnetic, to achieve these requirements.
In advanced micro-lithography machines a stable platform in six degrees-of-freedom (DOF) is required to support and isolate the complex lens system of the machine from vibrations. To date, micro-vibration problems within these machines could often be solved by means of adequate isolation of the equipment from the floor, i.e. the main plate is resiliently isolated from the floor, both passively and actively. This isolation is performed by three high-performance air bearings with additional linear actuators.

In order to provide an increased bandwidth solution and to reduce overall energy consumption, magnetic bearings are a possible substitute for the air bearings, e.g. in combination with mechanical means [9,10] or by fully magnetic means [11,12]. The support and vibration isolation are then achieved by passive gravity compensation using permanent magnets (PMs) and stabilization and accurate positioning by additional active electromagnets. In this respect, [11,12,13] describe similar vibration isolation systems for applications having smaller forces and similar or lower positioning requirements compared to the lithographic application.

The payload of the electromagnetic vibration isolator is in the order of thousands of kilograms and is supported by a passive permanent-magnet based gravity compensator. The high vertical force (F_z) needs to be combined with low spring stiffness (tens of Newtons per millimeter) to provide a low resonance frequency. This results in a high disturbance rejection even at low frequency levels.

IV. Magnetic Surface Charge Model

The high-precision actuators introduced in sections II and III are both ironless because iron is not suitable for these particular magnetic bearings. Hence, the magnetic field distribution can be obtained by summation of the fields of the individual permanent magnets.

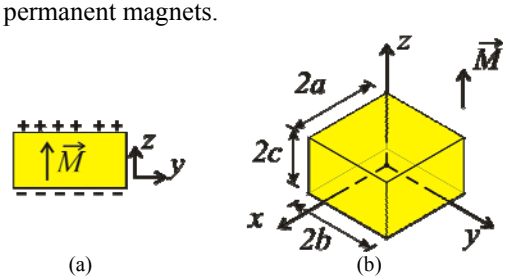

Fig. 3. (a) Schematic representation of the surface charge model and (b) definition of the variables of a single permanent magnet.

A. Magnetic flux density distribution of cuboidal permanent magnets

The magnetostatic magnetic field expression of the cuboidal permanent magnet in three dimensions is derived from Maxwell's equation under the assumption that the relative permeability is $\mu_r = 1$ both inside and outside the permanent magnet. Furthermore, it is assumed that the magnetization $\vec{M}$ of the permanent magnet is confined to its volume V with surface S, and falls abruptly to zero outside this volume.

The Maxwell equations can be solved by the introduction of either a scalar magnetic potential or a vector magnetic potential. In the first case an equivalent charge model of the permanent magnet, and in the second case an equivalent current model is obtained. For the cuboidal permanent magnets studied in the actuators presented in this paper the charge model is considered to be most convenient.

The magnetic flux density $\vec{B}$ may be written as

$$\vec{B}(\vec{r}) = \frac{\mu_0}{4\pi}\int_V \frac{\rho_m(\vec{r}\,')(\vec{r}-\vec{r}\,')}{|\vec{r}-\vec{r}\,'|^3}\mathrm{d}V + \frac{\mu_0}{4\pi}\int_S \frac{\sigma_m(\vec{r}\,')(\vec{r}-\vec{r}\,')}{|\vec{r}-\vec{r}\,'|^3}\mathrm{d}S, \quad (1)$$

$$\rho_m = -\nabla\cdot\vec{M}, \quad (2)$$

$$\sigma_m = \vec{M}\cdot\vec{n}. \quad (3)$$

where ρ_m is a volume charge distribution and σ_m is a surface charge distribution. For cuboidal magnets with uniform magnetization, i.e. $\nabla\cdot\vec{M} = 0$, only the surface charge density σ_m remains. The magnetic flux density distribution of a permanent magnet magnetized in the z-direction, as is shown in Fig. 3, is then given by [14]

$$B_x = \frac{B_r}{4\pi}\sum_{i=0}^{1}\sum_{j=0}^{1}\sum_{k=0}^{1}(-1)^{i+j+k}\log(R-T), \quad (4)$$

$$B_y = \frac{B_r}{4\pi}\sum_{i=0}^{1}\sum_{j=0}^{1}\sum_{k=0}^{1}(-1)^{i+j+k}\log(R-S), \quad (5)$$

$$B_z = \frac{B_r}{4\pi}\sum_{i=0}^{1}\sum_{j=0}^{1}\sum_{k=0}^{1}(-1)^{i+j+k}\operatorname{atan2}(ST, RU). \quad (6)$$

The variable B_r is the remanent magnetization of the permanent magnet, atan2 is a four-quadrant arctangent function and

$$R = \sqrt{S^2+T^2+U^2}, \quad (7)$$

$$S = x-(-1)^i a, \quad (8)$$

$$T = y-(-1)^j b, \quad (9)$$

$$U = z-(-1)^k c. \quad (10)$$

The magnet dimensions a, b and c are indicated in Fig. 3. By applying a four quadrant arctangent function in (6), the magnetic flux density is also correctly calculated inside the permanent magnet volume. Superposition can be used to model magnets with a magnetization vector which is not exactly along one of the Cartesian coordinate vectors albeit still under the assumption that the magnet has uniform magnetization ($\nabla\cdot\vec{M} = 0$).

As NdFeB permanent magnets exhibit a relative permeability of approximately 1.03-1.07, the assumption that $\mu_r = 1$ results

in a small modeling error. This error will be further discussed in section VII-A.

The method of images [15] provides means to obtain a correct field solution when infinitely large surfaces of unsaturated soft magnetic materials are present in the neighborhood of the permanent magnets. Even when the soft magnetic materials have finite dimensions and the magnetic paths are such that the field is confined to a small volume, the method of images provides a relatively accurate field solution [16]. This is beneficial for the analytical calculation of slotless magnet structures with back-iron.

For the ironless actuators discussed in this paper, the surface charge model has significant advantages with respect to other calculation methods. It provides accurate field expressions and it requires little computational effort, especially compared to FEM. More specifically, these analytical solutions are not mesh based, and therefore exhibit their high accuracy especially at large magnetic field gradients. Furthermore, the results are fully 3D which enables the analysis of non-repetitive structures or structures with strong end-effects. Another significant advantage above FEM or Fourier analysis is the ability to calculate the interaction force between individual magnets which are embedded in the same magnet array as will be discussed in section V.

B. Magnetic flux density distribution for planar Halbach arrays

The surface charge model allows to calculate magnetic flux density distributions of magnet assemblies including the edge-effects as all permanent magnets are individually modeled. In Figs. 6 and 8 the magnetic flux density distributions are shown of two different magnet arrays with quasi-Halbach magnetization which are shown in Figs. 5 and 7, respectively. These magnet arrays can be applied in both gravity compensators and planar actuators.

Both magnet arrays are similar, i.e. the permanent magnets in both arrays have the same dimensions, only the orientation of the magnet array with respect to the coordinate system is different. The magnet array in Fig. 7 has been rotated 45 mechanical degrees about the z-axis. In both cases the magnetic flux density has been predicted 4 mm below the array.

Fig. 6 shows the three components of the magnetic flux density distribution of the magnet array shown in Fig. 5. The components of the magnetic flux density distribution are sine waves in both the x- and y-directions. The waves of the B_x-, B_y- and B_z-components of the magnetic flux density distribution are shifted 90 electrical degrees with respect to each other. Considering this magnetic flux distribution, the obvious choice seems to apply square or round coils as indicated in Fig. 5 [2,6]. The size of this square coil is limited by the pole pitch τ of the magnet array. Depending on the position of the coil it will exert forces in the x-, y-, and z-directions.

However, when considering the magnetic flux distribution of the 45 mechanical degrees rotated magnet array (Fig. 7), which is shown in Fig. 8, it can be seen that also rectangular coils can be applied [3,4,5,7]. Due to the rotation with respect to the reference frame, the B_x-component of the magnetic flux density distribution is a sine wave in the x-direction and the B_y-component of the magnetic flux density distribution is a sine wave in the y-direction. Because of the rotation of the coordinate system, the spatial frequency of the sine waves is reduced. Hence, a new pole pitch τ_n can be introduced as indicated in Fig. 7

$$\tau_n = \frac{\tau}{\sqrt{2}}. \tag{11}$$

If the coil length of the rectangular coil

$$cl = 2n\tau_n, \tag{12}$$

where n is an integer and the coil is not near the edge of the magnet array, the field in the short sides of the rectangular coils is equal, and no force, but only a torque is acting on the short side. Consequently, the force production in the x- and y-directions can be physically decoupled for planar actuators with rectangular coils. Coil 1 in Fig. 7 can be displaced in the y-direction without change of the exerted force vector. The same holds for coil 2 when displaced in the x-direction. Because a significant higher force density can be obtained with these rectangular coils compared to round coils [17], this topology is chosen for the planar actuator which is discussed in this paper.

C. Demagnetization

Similar to fields solutions based on Fourier series and most FEM packages, it is also assumed in the surface charge model that permanent magnets operate above the knee point at the linear part of the demagnetization curve. The analytical surface charge model provides a powerful tool to calculate working points of the permanent magnets.

Especially in Halbach arrays demagnetization of the permanent magnets should be monitored closely as some parts of the magnets operate at high working points (even in the first quadrant) and some at low working points (near the third quadrant) of the demagnetization curve. Fig 9 shows two permanent magnets from the center of the Halbach magnet array which is shown in Fig. 5. The magnetic flux density distribution inside these magnets have been calculated with the surface charge model. The magnet parts which operate at low working points, i.e. $B_y < 0.25\text{T}$ and $B_z < 0.25\text{T}$ are identified in Figs. 9(a) and (b), respectively. It is observed that these regions occur in a thin layer near the edges of the magnets. To prevent demagnetization of these regions, the magnet material should be carefully selected for this magnet array.

V. Force between Magnets

The analytical field expressions for PMs can be used to obtain fast but accurate expressions for the interaction force between structures with permanent magnets. These force expressions are used to determine the force between magnet assemblies and the force in a magnet assembly, as used in the applications which are described in this paper.

A. The interaction force between cuboidal permanent magnets

Using the analytical field results presented in section IV-a, it is possible to derive the expressions for the force between permanent magnets either via the Lorentz force or via the virtual work method.

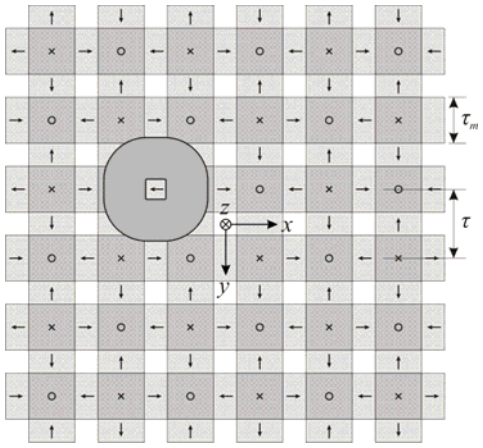

Fig. 5. Magnet array and square (or round) coils (bottom view).

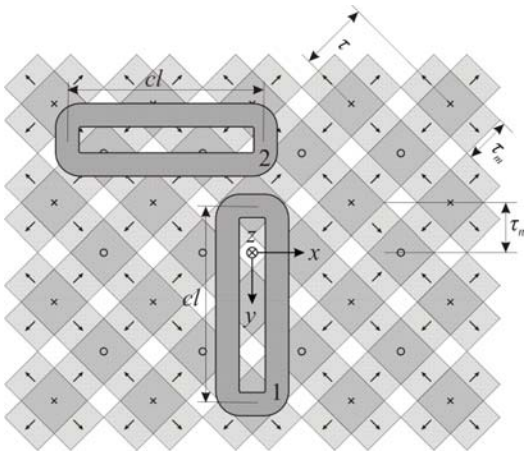

Fig. 7. Magnet array and two rectangular coils (bottom view).

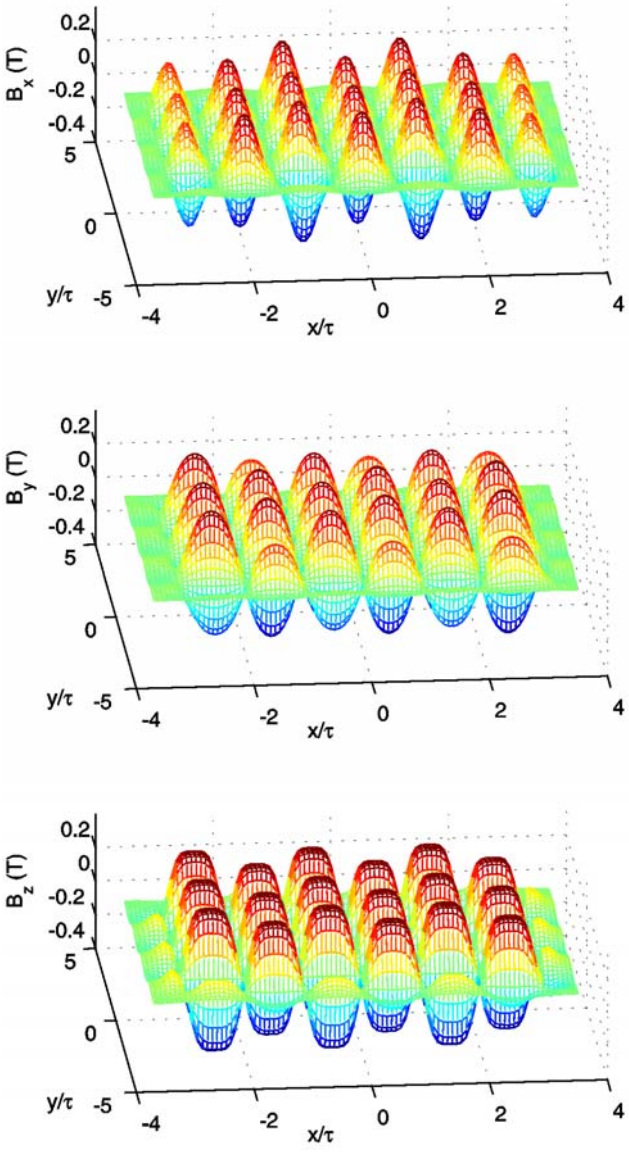

Fig. 6. Magnetic flux density distribution 4 mm below the magnet array shown in Fig. 5 predicted with the surface charge model (τ = 25 mm, τ_m/τ = 0.68, B_r = 1.24 T, magnet height: 7 mm).

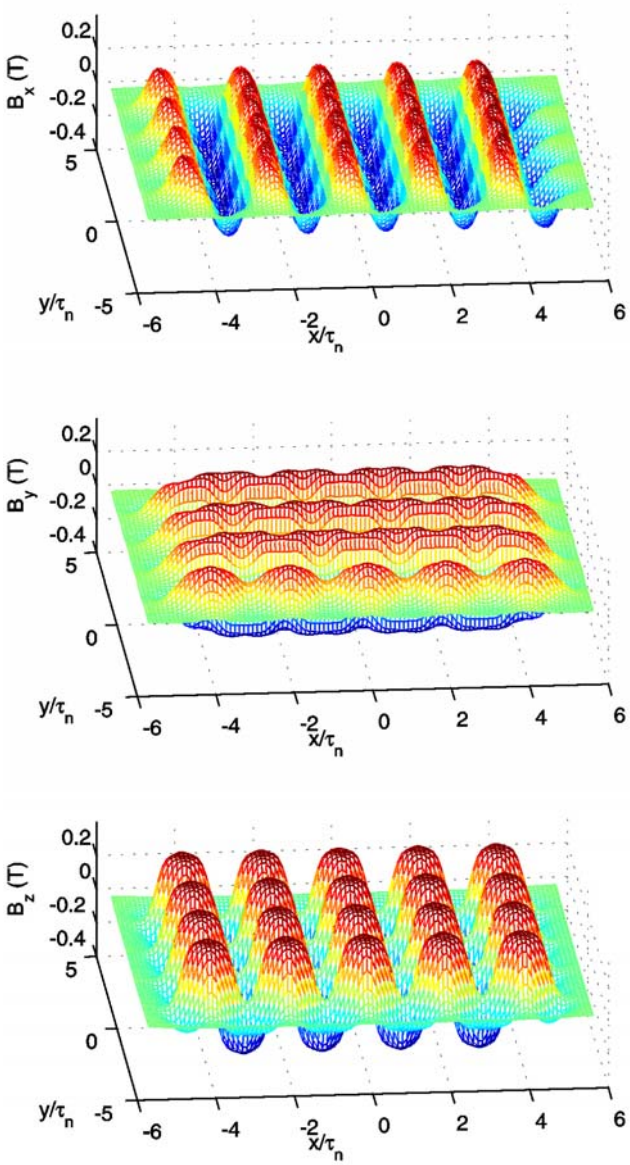

Fig. 8. Magnetic flux density distribution 4 mm below the magnet array shown in Fig. 6 predicted with the surface charge model (τ = 25 mm, τ_n = 17.7mm τ_m/τ = 0.68, B_r = 1.24 T, magnet height: 7 mm).

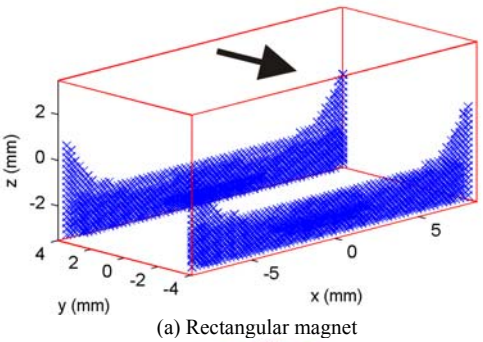

(a) Rectangular magnet

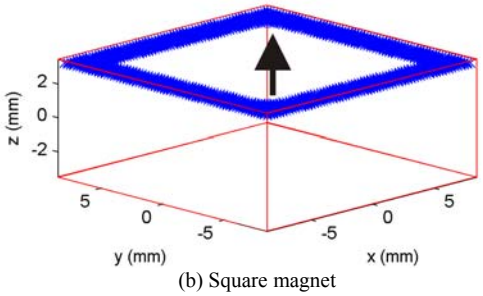

(b) Square magnet

Fig. 9. Parts within the magnets with an operating point with $B < 0.25$T when no external field is applied. The arrows indicate the magnetization direction and the field is sampled on a grid with 0.25mm elements.

By using the Lorentz force method the force on a magnetized body in the presence of an external field, B_{ext}, is given by

$$\vec{F} = \int_V \rho_m(\vec{r})\vec{B}_{ext}(\vec{r})\,\mathrm{d}v + \int_S \sigma_m(\vec{r})\vec{B}_{ext}(\vec{r})\,\mathrm{d}s. \tag{13}$$

Since the magnetization is assumed to be uniform the first term of (13) disappears [18] and only the second term remains. The surface charge density is written in terms of the remanence B_r by

$$\sigma_m = \vec{M}\cdot\hat{\vec{n}} = \frac{\vec{B_r}\cdot\hat{\vec{n}}}{\mu_0}. \tag{14}$$

The virtual work method is based on the total interaction energy in the system. The gradient of this energy results in the analytical force expressions [14]. The resulting equations are

$$W = \frac{1}{2}\int_V \vec{B}\cdot\vec{H}\,\mathrm{d}v = \int_{S_2}\int_{S_1} \frac{\sigma_{m_I}\sigma_{m_{II}}}{4\pi\mu_0 \vec{r}}\mathrm{d}s_1\mathrm{d}s_2, \tag{15}$$

$$\vec{T} = \int_V \vec{r}\times\vec{J}\times\vec{B}\mathrm{d}V. \tag{16}$$

Although both methods provide unique analytical expressions it is observed by the authors that they provide the same results. Analytical expressions for the interaction force between permanent magnets have been extensively described in [14] (virtual work) and [19] (magnetic nodes). The Lorentz

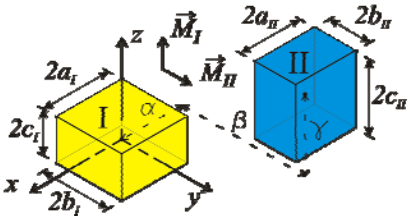

Fig. 10. Variables used in the calculation of interaction force between two cuboidal permanent magnets.

force expressions for two magnets which are magnetized along the z-axis are given by

$$\vec{F} = \frac{B_{r_I}B_{r_{II}}}{4\pi\mu_0}\sum_{i=0}^{1}\sum_{j=0}^{1}\sum_{k=0}^{1}\sum_{l=0}^{1}\sum_{p=0}^{1}\sum_{q=0}^{1}(-1)^{i+j+k+l+p+q}\vec{\psi}, \tag{17}$$

where B_{r_I} and $B_{r_{II}}$ are the respective remanent flux densities of both magnets and the vector $\vec{\psi}$ is an intermediate variable

$$\begin{aligned}\psi_x = &\frac{1}{2}(2TU\tan^{-1}\left(\frac{S}{U}\right)+2TU\tan^{-1}\left(\frac{ST}{UR}\right)\\ &+\left(U^2-T^2\right)\log\left(S+R\right)+S\left(2T\left(\log\left(R-T\right)-1\right)+R\right)),\end{aligned} \tag{18}$$

$$\begin{aligned}\psi_y = &\frac{1}{2}(2S\left(U\left(\tan^{-1}\left(\frac{T}{U}\right)+\tan^{-1}\left(\frac{ST}{UR}\right)\right)+T\log\left(R-S\right)\right)\\ &+T\left(R-2S\right)+\left(U^2-S^2\right)\log\left(T+R\right)),\end{aligned} \tag{19}$$

$$\begin{aligned}\psi_z = &S\coth^{-1}\left(\frac{S}{R}\right)U+T\coth^{-1}\left(\frac{T}{R}\right)U-\\ &RU+ST\tan^{-1}\left(\frac{ST}{UR}\right).\end{aligned} \tag{20}$$

The equations above are suitable for analyzing magnet arrays with magnetization along a single axis. In quasi-Halbach arrays there are three axes along which the magnets are magnetized. For simulating such a structure, the analytical expressions for interaction force between perpendicularly magnetized permanent magnets are necessary. In [20] the analytical force expressions for perpendicularly magnetized permanent magnets are derived using the virtual work method. In [21] the Lorentz force method is used to obtain the analytical expressions

$$\vec{F} = \frac{B_{r_I}B_{r_{II}}}{4\pi\mu_0}\sum_{i=0}^{1}\sum_{j=0}^{1}\sum_{k=0}^{1}\sum_{l=0}^{1}\sum_{p=0}^{1}\sum_{q=0}^{1}(-1)^{i+j+k+l+p+q}\vec{\psi}, \tag{21}$$

with

$$\begin{aligned}\psi_x = &\frac{1}{2}\Bigg[\left(\tan^{-1}\left(\frac{U}{S}\right)+\tan^{-1}\left(\frac{TU}{SR}\right)\right)S^2+2TS\\ &-3US-2ST\log\left(U+R\right)-2T^2\tan^{-1}\left(\frac{S}{T}\right)+\\ &U\Big(U\left(2\tan^{-1}\left(\frac{S}{U}\right)+\tan^{-1}\left(\frac{U}{S}\right)+\tan^{-1}\left(\frac{ST}{UR}\right)\right)\\ &-2T\log\left(S+R\right)+2S\log\left(R-T\right)\Big)+T^2\tan^{-1}\left(\frac{SU}{TR}\right)\Bigg],\end{aligned} \tag{22}$$

$$\begin{aligned}\psi_y = &\frac{1}{2}\Big[U\left(R-2S\right)+\left(T^2-S^2\right)\log\left(U+R\right)\\ &+2S\left(T\left(\tan^{-1}\left(\frac{U}{T}\right)+\tan^{-1}\left(\frac{SU}{TR}\right)\right)+U\log\left(R-S\right)\right)\Big],\end{aligned} \tag{23}$$

$$\begin{aligned}\psi_z = &\frac{1}{2}\Big[T\left(R-2S\right)+\left(U^2-S^2\right)\log\left(T+R\right)\\ &+2S\left(U\left(\tan^{-1}\left(\frac{T}{U}\right)+\tan^{-1}\left(\frac{ST}{UR}\right)\right)+T\log\left(R-S\right)\right)\Big].\end{aligned} \tag{24}$$

$$\begin{aligned}S &= \alpha-(-1)^i a_I+(-1)^j a_{II},\\ T &= \beta-(-1)^k b_I+(-1)^l b_{II},\\ U &= \gamma-(-1)^p c_I+(-1)^q c_{II},\\ R &= \sqrt{S^2+T^2+U^2}.\end{aligned} \tag{25}$$

The magnet dimensions $a_I \ldots c_{II}$ and displacement variables α, β and γ are shown in Fig. 10.

The analytical methods described above are based on a mathematical approach and therefore have no physical meaning. This is extensively discussed in [22] for several analytical and numerical calculation methodologies. As a result the analytical model is only globally equivalent to the original system and does not represent the actual distribution of forces within the permanent magnets.

The analytical expressions derived above can be implemented to obtain the force between or even inside large permanent magnet arrays. This is elaborated on in sections V-B and V-C.

B. Interaction Force in the Gravity Compensator

The passive gravity compensator is part of the electromagnetic vibration isolator and the gravity compensation is performed by permanent magnet structures. A topology search focused on maximizing the force density of these structures was presented in [23]. A high force density reduces the volume of the gravity compensator and, in this way, creates space for additional electromagnetic actuators and sensors within the specified vibration isolator volume. The topology which resulted from [23] is used here to perform a number of simulations which characterize some of the most important parameters of the gravity compensator and demonstrate the capabilities of the surface charge model. Although the stroke is very small (less than 1 mm), it is important that the force that is exerted does not change significantly along this stroke. Furthermore, it is important that the spring stiffness is accurately calculated for reasons discussed in section III.

Fig. 11 shows a layout and dimensions for a gravity compensator with a 6x6 quasi-Halbach magnet structure. The analytically obtained vertical interaction force as function of horizontal displacement is shown in Fig. 12. One quadrant of the displacement is shown (only positive x and y), since the other three quadrants exhibit similar behavior due to the symmetric structure of the device. The figure demonstrates

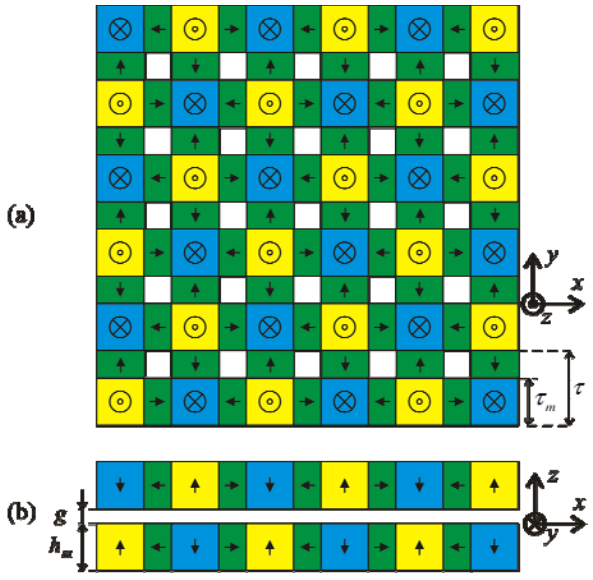

Fig. 11. Top view (a) and side view (b) of a double sided quasi-Halbach structure for the gravity compensator with τ_m =11.77 mm, τ =17.65 mm and h_m =10.00 mm.

that the influence of the displacement on the interaction force is relatively small when compared to its absolute value of 4.4kN.

The stiffness is expressed in a 3x3 Jacobian matrix which describes the coupling between force and displacement vectors along the three Cartesian directions. It is given by

$$\mathbf{K} = -\begin{pmatrix} \frac{\partial F_x}{\partial x} & \frac{\partial F_x}{\partial y} & \frac{\partial F_x}{\partial z} \\ \frac{\partial F_y}{\partial x} & \frac{\partial F_y}{\partial y} & \frac{\partial F_y}{\partial z} \\ \frac{\partial F_z}{\partial x} & \frac{\partial F_z}{\partial y} & \frac{\partial F_z}{\partial z} \end{pmatrix}. \tag{26}$$

By using (17-25) in (26) analytical expressions for the entries in the stiffness matrix are obtained in a single calculation. This is an advantage over FEM, which determines the spring stiffness by the numerical derivative of the force to the displacement. At least three individual simulations would be necessary to obtain 9 values for the stiffness matrix.

With the two parts of the gravity compensator are not horizontal displaced only $K_{xx}= \partial Fx/\partial x$, $K_{yy}= \partial F_y/\partial y$ and $K_{zz}= \partial F_z/\partial z$ are nonzero. Fig. 13 shows the influence of horizontal displacement on the most important stiffness value

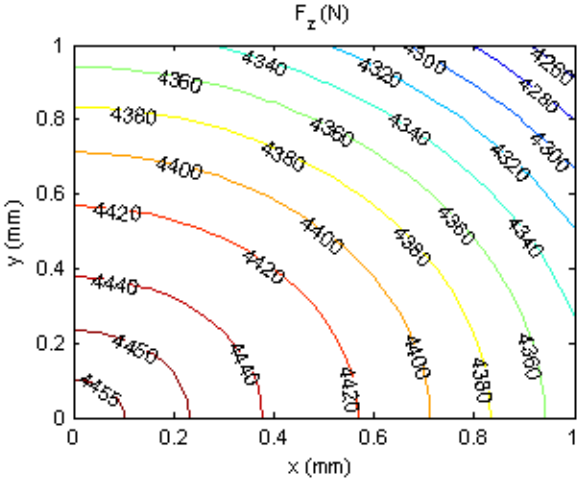

Fig. 12. Influence of horizontal displacement on the vertical interaction force F_z.

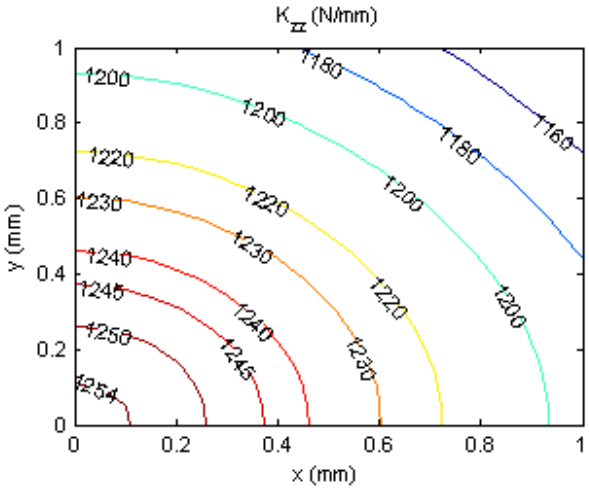

Fig. 13. Influence of horizontal displacement on the vertical spring stiffness K_{zz} which is expressed in N/mm.

is fully analytically obtained. The other stiffness values vary as well, but are not shown in this article.

When compared to the requirements in section III, it can be concluded that the topology that is presented in this article is suboptimal. The force level is under specification and the stiffness level is over specification. Optimization of the structure is therefore considered necessary to obtain a design that is feasible for lithographic application. The fast-solving analytical 3D surface charge model is very suitable to be used in such routine.

C. Force inside a magnet assembly

The calculation of the forces between permanent magnets inside a magnet array is important to estimate the deformation of the magnet assembly as it will change the airgap and give rise to deviation of the force and torque.

As FEM applies the virtual work method or the Maxwell stress tensor method to calculate the force on an object, it should be surrounded by a layer of air. As the permanent magnets in the planar Halbach arrays are typically positioned at 50 µm to 100 µm from each other, the mesh size in the layer of air, which should be chosen equal to or smaller than the thickness of the layer of air, becomes very small compared to the problem size. As a result, the mesh will be extremely large, and it is unpractical to solve this problem with FEM.

Instead, the force expressions derived from the magnetic surface charge model are used to calculate the force inside a magnet assembly. Fig. 14 shows a Halbach array with the forces (in N) in the (x, y, z) - direction beside the arrows. Note that the force is not indicated for each magnet and that the total force acting on the permanent magnet array equals zero. The z-component of the force acting on the permanent magnets magnetized in the z-direction is most significant and equal to approximately 166 N. For a Halbach array consisting of 11x11 permanent magnets alternatively magnetized in the z-direction (as used in the planar actuator presented in [5]), this force component increases with less than 0.1 %. Hence, the interaction force is independent of the number of magnets in the array.

The deformation of a 5 mm thick aluminum carrier on which a Halbach permanent magnet array is glued, which is similar to the magnet array used in the planar actuator, is calculated by means of mechanical FEM simulations in Marc/Mentat [24]. Several assumptions and simplifications are made of which the most important assumption was that the magnets itself do not contribute to the stiffness of the construction. The results are shown in Fig. 15. The outer edges of the magnet plate bend downwards by approximately 0.2 mm with respect to the center of the magnet plate. An impression of a cross-section of the deformed aluminum plate with the permanent magnets is shown in Fig. 16. These results are similar to the data obtained from measurements on the magnet assembly during manufacturing. This deformation is significant considering the accuracy demanded by the applications for which these types of planar actuators are being designed. To reduce the deformation of the magnet array glued on the 5 mm thick aluminum plate, the translator of the planar actuator has been reinforced with an aluminum structure with a high stiffness.

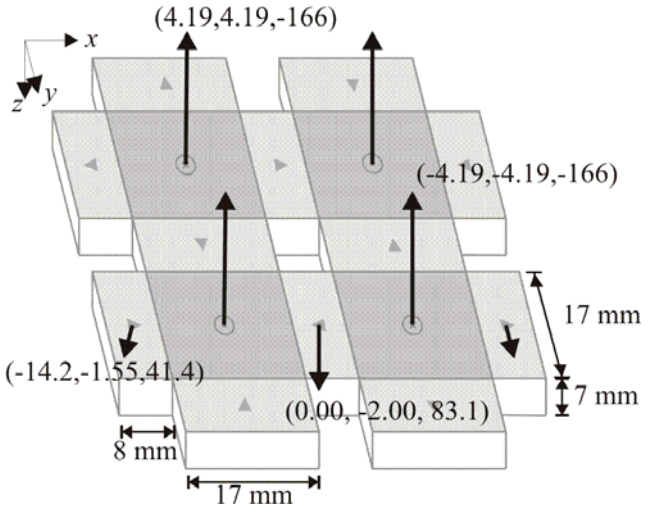

Fig. 14. Forces acting on the permanent magnets in the Halbach array, the numbers beside the vector indicate the force in the (x, y, z)-direction.

VI. Force between a magnet Assembly and a Coil

As the planar actuator has a coreless structure, the force acting on a magnet assembly due to the current in a coil is calculated using the Lorentz force equation

$$\vec{F} = -\int_V \vec{J} \times \vec{B} \mathrm{d}V, \tag{27}$$

where $\vec{J}$ is the current distribution in the coil, $\vec{B}$ is the magnetic flux density due to the magnet and V is the volume of the coil. The torque on the magnet assembly is given by

$$\vec{T} = -\int_V \vec{r} \times \vec{J} \times \vec{B} \mathrm{d}V, \tag{28}$$

where $\vec{r}$ is the vector to the point about which the torque is computed. These integrals can be solved numerically using a cuboidal mesh as shown in Fig. 17. By applying the appropriate coordinate transformations, the Lorentz force and torque integrals can be solved for arbitrary position and orientation of the magnet assembly and coil. A disadvantage of calculating the force and torque on a coil by numerically

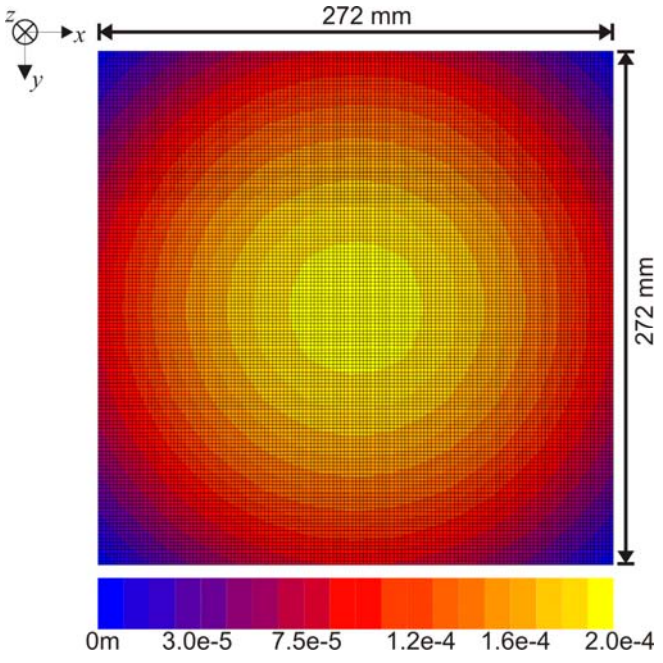

Fig. 15. Deformation of the magnet plate. The legend indicates local displacement in the z-direction.

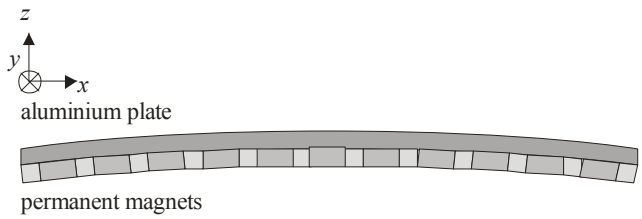

Fig. 16. Impression of a cross-section of the deformed aluminum plate with the array of permanent magnets.

evaluating the integral over its volume is the computation time (typically 10-20 seconds per coil).

In Fig. 18, the coil of the realized planar actuator is indicated for which the force and torque profiles have been measured using a 6-DOF loadcell. The profiles have been measured with a DC coil current of 1 A and are shown in Figs. 19 and 20, respectively. The position of the magnet array is indicated by the vector $\vec{p}$, The measured force and torque are expressed in the coordinate system indicated in the mass centre point of the magnet array (with superscript *m*), to show the decoupling between the force components in the *xy*-plane. This decoupling is clearly visible in Fig. 19. Contrary to a moving-coil planar actuator in which the coil is positioned at a fixed distance to the mass centre point of the translator, Fig. 20 shows that the torque components in a moving-magnet planar actuator are depending on both the absolute and relative position of the magnet array with respect to the coil. The measured profiles are in good agreement with prediction with the surface charge based model as shown in Fig. 21 in which they are compared for the torque component T_x at p_y = 8.3 mm.

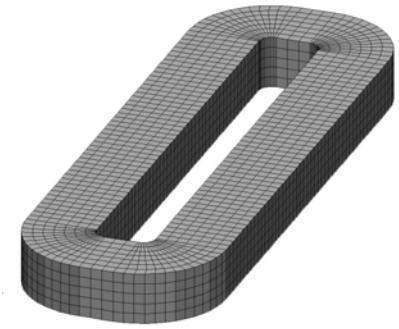

Fig. 17. Coil with cuboidal mesh.

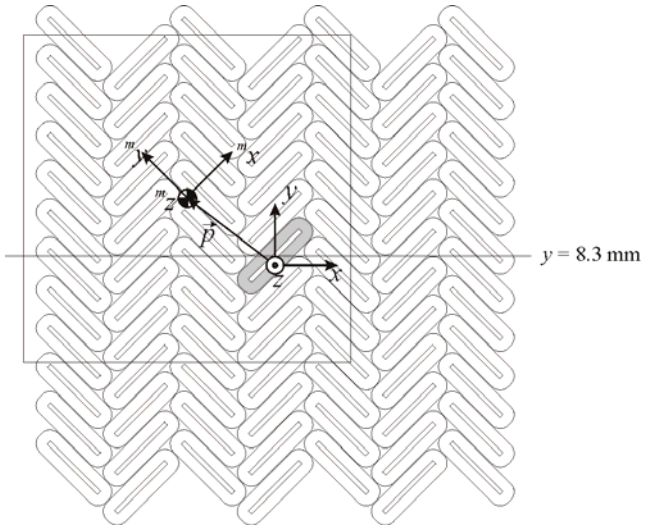

Fig. 18. Coil for which the force and torque profiles are shown in Figs. 19 and 20. The square indicates the edge of the magnet array.

VII. HARMONIC MODEL

The surface charge model provides the user with the possibility to calculate the fields of permanent magnets which are positioned at arbitrary points in space. This is convenient for actuators with a small stroke such as gravity compensators, but in most long-stroke actuators a periodical permanent magnet array is present which can also be accurately described as a boundary value problem and Fourier series. The application of these harmonic models can result in significant reduction of the calculation time, as the calculation time is only dependent on the number of harmonics taken into account instead of the number of magnets in the magnet array. Furthermore, in the harmonic models the relative permeability of the permanent magnets can be included.

The harmonic model [25] which is applied in the analysis of the planar actuator assume an infinitely large magnet array and have a limited number of degrees-of-freedom in order to minimize the calculation time. This results in two model limitations. Firstly, the edge effects of the magnet array are not included. However, the edge effects are of minor importance in many design steps, such as the optimization of the sizes of the magnets and coils. Secondly, the model cannot be used for simulation of the planar actuator with a controller for all six degrees-of-freedom because the rotational movements are fixed.

A. Magnetic flux density

The magnetic flux density distribution of a planar Halbach array is calculated by dividing the problem into three regions, as shown in Fig. 22. Regions 1 and 3 are in air and region 2 contains the permanent magnets. The empty spaces in the magnet array are assumed to consist of unmagnetized material with the same relative permeability as the permanent magnets. The remanent magnetization vector $\vec{M}$ of the magnet array which is shown in Fig. 5 can be expressed as

$$\vec{M} = \frac{B_r}{\mu_0}\sum_{k=1}^{\infty}\sum_{l=1}^{\infty}\begin{bmatrix} -a(k)b(l)\cos\left(\frac{k\pi x}{\tau}\right)\sin\left(\frac{l\pi y}{\tau}\right) \\ -b(k)a(l)\sin\left(\frac{k\pi x}{\tau}\right)\cos\left(\frac{l\pi y}{\tau}\right) \\ -b(k)b(l)\sin\left(\frac{k\pi x}{\tau}\right)\sin\left(\frac{l\pi y}{\tau}\right) \end{bmatrix}, \tag{29}$$

where B_r is the remanent flux density, k and l are the harmonic numbers for the x- and y-directions respectively, and the functions a and b are given by

$$a(k) = \frac{4}{k\pi}\cos\left(\frac{k\tau_m\pi}{2\tau}\right)\sin\left(\frac{k\pi}{\tau}\right), \tag{30}$$

$$b(k) = \frac{4}{k\pi}\sin\left(\frac{k\tau_m\pi}{2\tau}\right)\sin\left(\frac{k\pi}{\tau}\right), \tag{31}$$

where τ is the pole pitch and τ_m is the length of the side of the magnet magnetized in the z-direction.

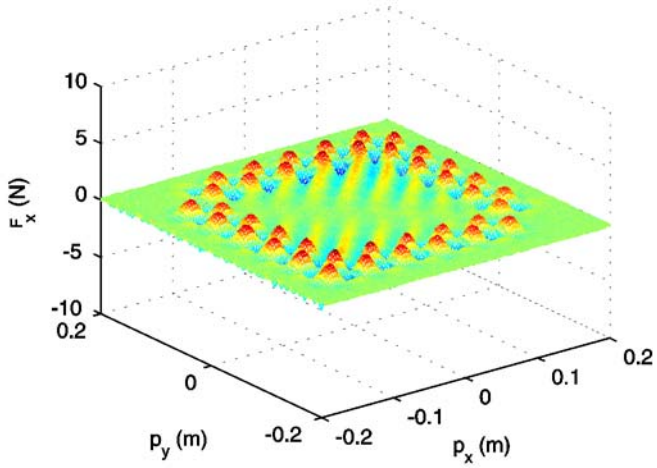

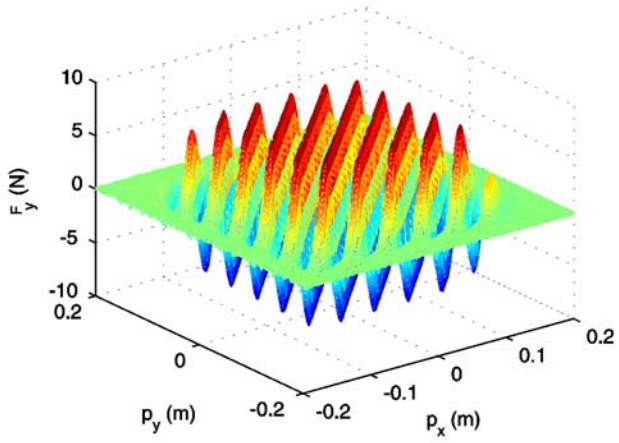

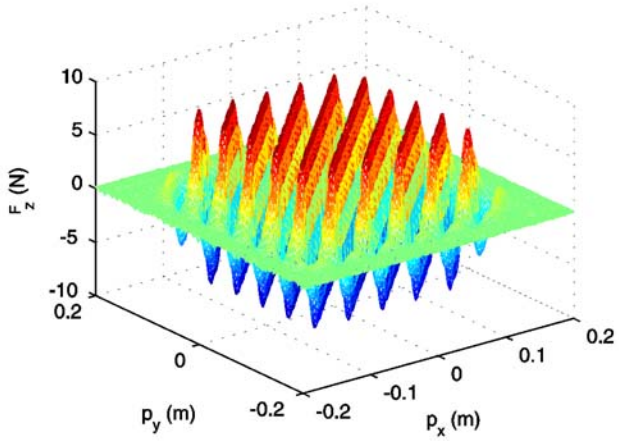

Fig. 19. Force acting on the translator of the planar actuator due to a single coil (Fig. 18).

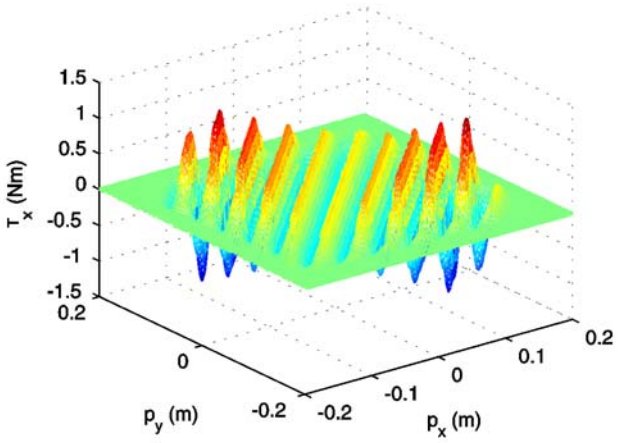

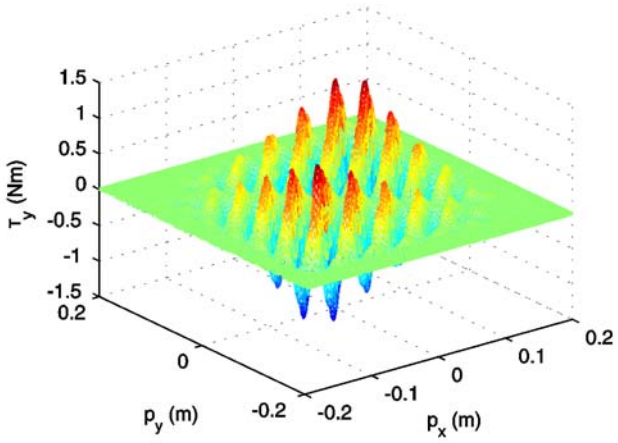

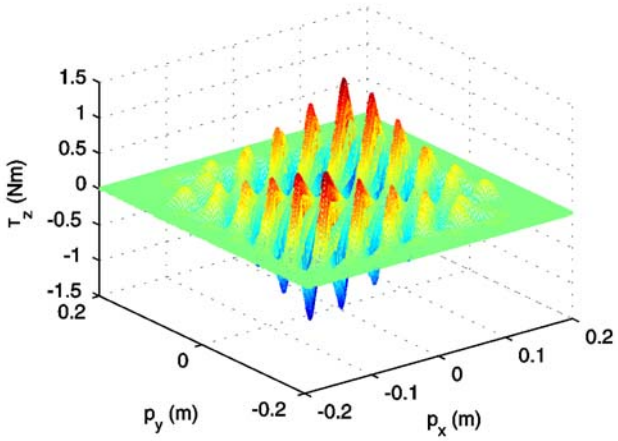

Fig. 20. Torque acting on the translator of the planar actuator due to a single coil (Fig. 18).

TABLE 1. MAGNETIC FIELD EQUATION IN THE RESPECTIVE REGIONS OF THE MODEL IN FIG. 22

Region 1	Region 2	Region 3
$\nabla \times \vec{H}_1 = \vec{0}$	$\nabla \times \vec{H}_2 = \vec{0}$	$\nabla \times \vec{H}_3 = \vec{0}$
$\nabla \cdot \vec{B}_1 = 0$	$\nabla \cdot \vec{B}_2 = 0$	$\nabla \cdot \vec{B}_3 = 0$
$\vec{B}_1 = \mu_0 \vec{H}_1$	$\vec{B}_2 = \mu_0 \vec{H}_2 + \mu_0 \mu_r \vec{M}$	$\vec{B}_3 = \mu_0 \vec{H}_3$
$\vec{H}_1 = -\nabla \Psi_1$	$\vec{H}_1 = -\nabla \Psi_2$	$\vec{H}_1 = -\nabla \Psi_3$
$\nabla^2 \Psi_1 = 0$	$\nabla^2 \Psi_1 = \nabla \cdot \vec{M}$	$\nabla^2 \Psi_3 = 0$

TABLE 2. BOUNDARY CONDITIONS

$z = \infty$	$z = m_t$	$z = m_b$	$z = -\infty$
$\Psi_1 = 0$	$H_{1,x} = H_{2,x}$	$H_{2,x} = H_{3,x}$	$\Psi_3 = 0$
	$H_{1,y} = H_{2,y}$	$H_{2,y} = H_{3,y}$	
	$B_{1,z} = B_{2,z}$	$B_{2,z} = B_{3,z}$	

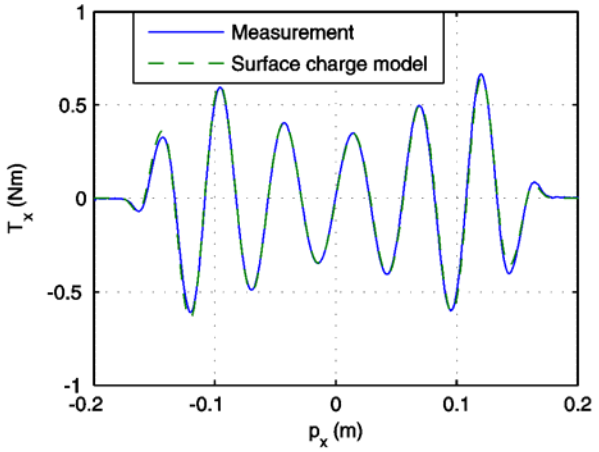

Fig. 21 Measurement and simulation with the surface charge model of the torque component T_x acting on the translator of the planar actuator due to a single coil (Fig. 18), p_y = 8.3 mm.

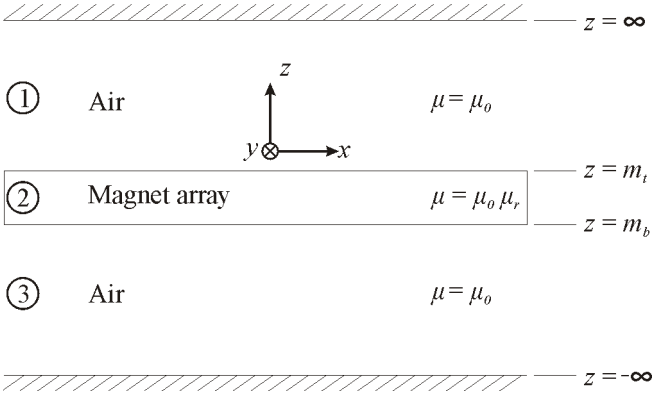

Fig. 22. 3-D space with magnet array divided into three regions.

The governing equations in the three regions and their boundary conditions are summarized in Tables 1 and 2. The scalar potential Ψ is introduced according to

$$\vec{H} = -\nabla\Psi \tag{32}$$

to solve these equations. The solutions of the Laplace equations in regions 1 and 3, taking into account the boundary conditions $\Psi_1(z=\infty)=0$ and $\Psi_3(z=-\infty)=0$), and the Poisson equation in region 2 are given by

$$\Psi_1 = \sum_{k=1}^{\infty}\sum_{l=1}^{\infty} K_1 e^{-\lambda z}\sin\left(\frac{k\pi x}{\tau}\right)\sin\left(\frac{l\pi y}{\tau}\right), \tag{33}$$

$$\Psi_2 = \sum_{k=1}^{\infty}\sum_{l=1}^{\infty}\left(K_{21}e^{-\lambda z} + K_{22}e^{\lambda z} - \frac{B_r a(l)b(k)l\tau + B_r a(k)b(l)k\tau}{\mu_0\mu_r\pi(k^2+l^2)}\right) \cdot\sin\left(\frac{k\pi x}{\tau}\right)\sin\left(\frac{l\pi y}{\tau}\right), \tag{34}$$

$$\Psi_3 = \sum_{k=1}^{\infty}\sum_{l=1}^{\infty} K_3 e^{\lambda z}\sin\left(\frac{k\pi x}{\tau}\right)\sin\left(\frac{l\pi y}{\tau}\right), \tag{35}$$

where K_1, K_{21}, K_{22} and K_3 are constants and

$$\lambda = \sqrt{\left(\frac{k\pi}{\tau}\right)^2 + \left(\frac{l\pi}{\tau}\right)^2}. \tag{36}$$

The constants can be calculated with the boundary conditions given in Table 2. The resulting expression for the magnetic flux density in the region of interest, region 3, is equal to

$$\vec{B}_3(\vec{x}) = -\mu_0\nabla\Psi_3$$

$$= -\mu_0\sum_{k=1}^{\infty}\sum_{l=1}^{\infty} K_3 e^{\lambda z}\begin{bmatrix}\frac{k\pi}{\tau}\cos\left(\frac{k\pi x}{\tau}\right)\sin\left(\frac{l\pi y}{\tau}\right)\\ \frac{l\pi}{\tau}\sin\left(\frac{k\pi x}{\tau}\right)\cos\left(\frac{l\pi y}{\tau}\right)\\ \lambda\sin\left(\frac{k\pi x}{\tau}\right)\sin\left(\frac{l\pi y}{\tau}\right)\end{bmatrix}, \tag{37}$$

where

$$K_3 = \frac{B_r e^{-m_b\lambda}\left(e^{m_b\lambda} - e^{m_t\lambda}\right)}{\left(k^2+l^2\right)\pi\lambda\left(e^{2m_b\lambda}(\mu_r-1)^2 - e^{2m_t\lambda}(\mu_r+1)^2\right)\mu_0} \cdot\left(k\lambda\left(e^{m_b\lambda}(\mu_r-1)+e^{m_t\lambda}(\mu_r+1)\right)\tau a(l)b(k) + \left(k^2+l^2\right)\pi\left(e^{m_b\lambda}(\mu_r-1)-e^{m_t\lambda}(\mu_r+1)\right)a(l)a(k) + l\lambda\left(e^{m_b\lambda}(\mu_r-1)+e^{m_t\lambda}(\mu_r+1)\right)\tau b(l)a(k)\right), \tag{38}$$

where m_t and m_b are the z-coordinates of the magnets.

The error which results from the assumption in the surface charge model that the relative permeability is equal to 1 can be evaluated with (37). In Fig. 23, the reduction of different harmonics of the z-component of the magnetic flux density is shown for magnet arrays with different values of the relative permeability with respect to a magnet array with μ_r=1. The figure shows that for an array with high quality NdFeB magnets with μ_r=1.03, the magnetic surface charge predicts a 1.5% too high magnetic flux density. For magnets with μ_r=1.10, the error is approximately 5%. Similar results can be

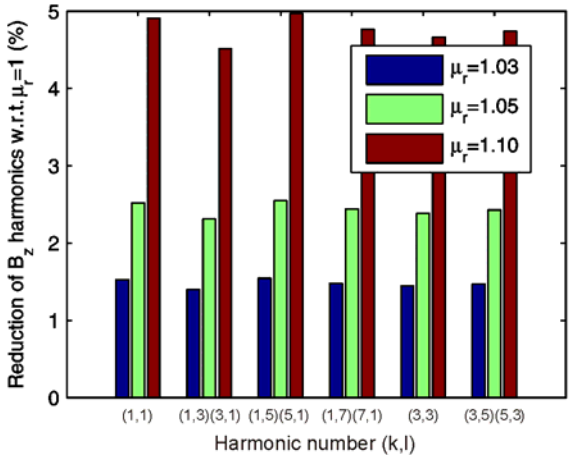

Fig. 23. Error resulting from the error in relative permeability μ_r.

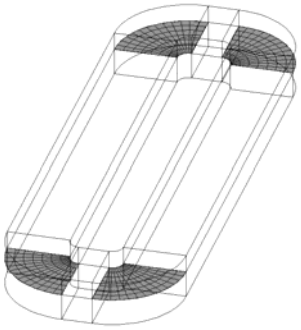

Fig. 24. Coil mesh used for the force and torque calculations with the harmonic model.

obtained for the *x*- and *y*-components of the magnetic flux density.

B. Force and torque calculation

Similar to the planar actuator model based on surface charges, the force and torque in the harmonic model are calculated with the Lorentz force law. When the rotation angles of the magnet array are fixed, i.e. no rotations about the *x*- and *y*-axes, and the coils are either not rotated (Fig. 5) or 45 degrees rotated (Fig. 7) about the *z*-axis, the Lorentz force and torque equations can be solved mainly analytically. The integrals are solved analytically in the straight segments of the coils and only have to be approximated numerically in the corner segments of the coil. The numerical approximation is only necessary for the integrals over *x* and *y*, and hence, only a numerical surface integral has to be solved. This is illustrated in Fig. 24 which shows an example of the mesh used for the force and torque calculation with the harmonic model.

Because of the largely analytical solution of the force and torque, the calculation time of the Harmonic planar actuator model is approximately 1 second for a full planar actuator topology. Such a short calculation time is very convenient for the evaluation of a many planar actuator topologies. For each topology, the force and torque is typically calculated at 2000-5000 different positions of the magnet array.

C. Analytical model

The commutation algorithm of the planar actuator has to decouple the force and torque and the coil currents. Therefore, the algorithm needs a model of the force and torque in the actuator which evaluates on a microsecond scale and which incorporates all degrees-of-freedom. This analytical model is derived from the harmonic model and only takes into account the first harmonic of the magnetic flux density. The coil is modeled by four straight surface currents to obtain a fully analytical solution.

Fig. 25 shows a bottom and side view of a planar magnet array, a coil and the coil model with surface currents. The coil has a length *cl*, a width *w* and a conductor bundle width *cb*. The vector $\vec{p}$ is the vector which defines the position of the magnet array with respect to the coordinate system of the stator. The magnetic flux density expression for the magnet array is derived from (37) using a coordinate transformation

$$\vec{B}_3(\vec{x},\vec{p}=\vec{0})=\begin{bmatrix} -\frac{B_{xy}}{\sqrt{2}}e^{\frac{\sqrt{2}\pi}{\tau}z}\sin\left(\frac{\sqrt{2}\pi x}{\tau}\right) \\ \frac{B_{xy}}{\sqrt{2}}e^{\frac{\sqrt{2}\pi}{\tau}z}\sin\left(\frac{\sqrt{2}\pi y}{\tau}\right) \\ \frac{1}{2}B_z e^{\frac{\sqrt{2}\pi}{\tau}z}\left(\cos\left(\frac{\sqrt{2}\pi x}{\tau}\right)-\cos\left(\frac{\sqrt{2}\pi y}{\tau}\right)\right) \end{bmatrix}, \quad (39)$$

where B_{xy} and B_z are the amplitude of the mean value of the first harmonic of the magnetic flux density components in the cross section of the coil. It can be derived that

$$B_z=\sqrt{2}B_{xy}, \quad (40)$$

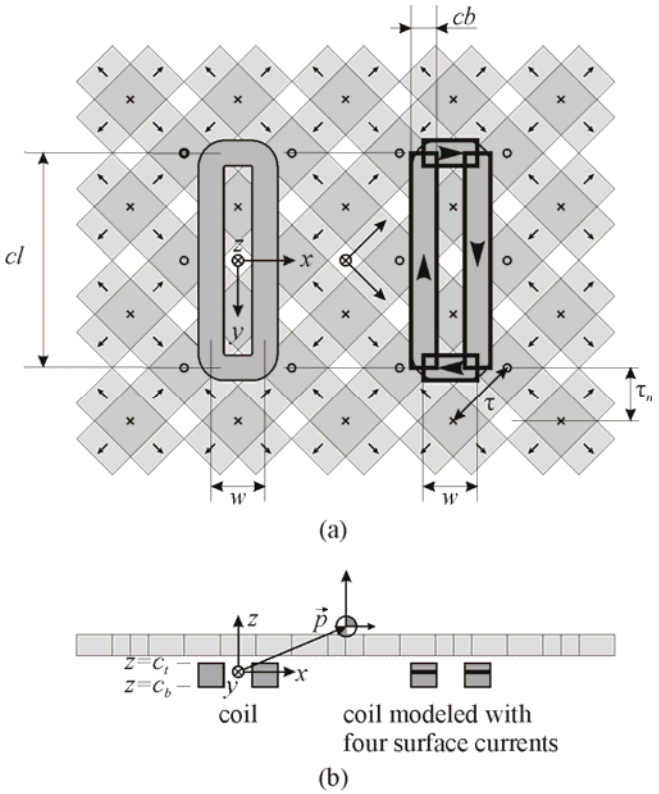

Fig. 25. Bottom (a) and side view (b) of a planar magnet array, a coil and the coil model with surface currents.

The location of the surface currents in the *z*-direction, z_{sc}, can be determined by calculating the effective torque arm in the *z*-direction and is given by [25]

$$z_{sc}=c_t+\frac{(c_b-c_t)e^{\lambda c_b}}{e^{\lambda c_b}-e^{\lambda c_t}}-\frac{1}{\lambda}, \quad (41)$$

where c_b and c_t are the *z*-coordinate of the bottom and top of the coil as indicated in Fig. 25. Because only the first harmonic is considered

$$\lambda=\frac{\sqrt{2}\pi}{\tau}. \quad (42)$$

Integration of the Lorentz force and torque over the surface currents for a coil which centre is located in *(x, y, z = z_{sc} = 0)*

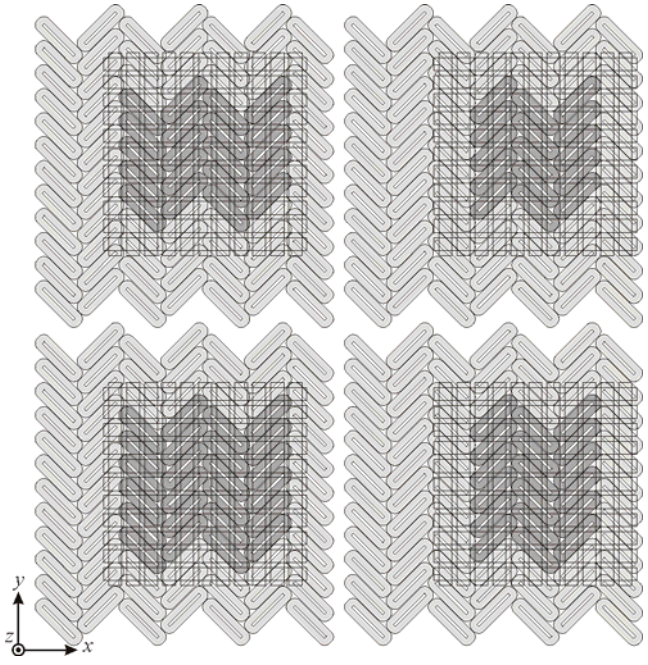

Fig. 26. Switching of the coils in the planar actuator.

and with $w = \tau_n$, $cl = 4\tau_n$, and $cb = \tau_n/2$, results in

$$F_x = -2\sqrt{2}B_z i\tau e^{-\frac{\sqrt{2}\pi}{\tau}p_z} \sin\left(\frac{\sqrt{2}\pi(p_x - x)}{\tau}\right), \quad (43)$$

$$F_y = 0, \quad (44)$$

$$F_z = -4B_{xy} i\tau e^{-\frac{\sqrt{2}\pi}{\tau}p_z} \cos\left(\frac{\sqrt{2}\pi(p_x - x)}{\tau}\right), \quad (45)$$

$$T_x = \left(y - p_y\right)F_z - \sqrt{2}B_{xy}\, i\tau^2 e^{-\frac{\sqrt{2}\pi}{\tau}p_z} \sin\left(\frac{\sqrt{2}\pi(p_y - y)}{\tau}\right), \quad (46)$$

$$T_y = \left(p_x - x\right)F_z - p_z F_x + F_x \frac{B_{xy}\left(\pi - 4\right)\tau}{4B_z\pi}, \quad (47)$$

$$T_z = F_x\left(p_y - y\right). \quad (48)$$

The torque expressions show that the torque cannot be expressed as an arm multiplied by a force and that the distribution of the force over the coil changes with the position of the magnet array.

The model can be extended to six degrees-of-freedom by Taylor expansion to the rotation angles.

VIII. Simulation of Commutated Planar Actuator

An analytical model based on surface currents, such as derived in the previous section, is used to commutate the planar actuator. The wrench $\vec{w}$ is the vector which contains the total force and torque acting on the translator

$$\vec{w} = \begin{bmatrix} F_x & F_y & F_z & T_x & T_y & T_z \end{bmatrix}^{\bullet}. \quad (49)$$

The wrench vector for a planar actuator with n coils is given by

$$\vec{w} = \begin{bmatrix} F_{1,x}(\vec{p}) & F_{2,x}(\vec{p}) & \dots & F_{n,x}(\vec{p}) \\ F_{1,y}(\vec{p}) & F_{2,y}(\vec{p}) & \dots & F_{n,y}(\vec{p}) \\ F_{1,z}(\vec{p}) & F_{2,z}(\vec{p}) & \dots & F_{n,z}(\vec{p}) \\ T_{1,x}(\vec{p}) & T_{2,x}(\vec{p}) & \dots & T_{n,x}(\vec{p}) \\ T_{1,y}(\vec{p}) & T_{2,y}(\vec{p}) & \dots & T_{n,y}(\vec{p}) \\ T_{1,z}(\vec{p}) & T_{2,z}(\vec{p}) & \dots & T_{n,z}(\vec{p}) \end{bmatrix} \begin{bmatrix} i_1 \\ i_2 \\ \vdots \\ i_n \end{bmatrix} = \Gamma(\vec{p})\vec{i}, \quad (50)$$

where $\vec{i}$ is the current vector containing the currents in the respective coils. The matrix $\Gamma(\vec{p})$ is a mapping of the current in the coils on the force and torque exerted on the translator as a function of the position and the orientation of the translator in six DOF $\vec{p}$. The force and torque functions are expressed on a per Ampere base and calculated by the analytical model.

The controller of the planar actuator calculates the desired wrench setpoint every sample time by inverting $\Gamma(\vec{p})$. This wrench setpoint has to be converted to current settings for the power amplifier. As the system is over-actuated, i.e. a six degree-of-freedom wrench is made by 24 coils, there is an infinite number of solutions for the inverse of $\Gamma(\vec{p})$. A convenient solution is to search for the inverse with minimum power dissipation in the coils. This is similar to minimizing the 2-norm of the current vector $\vec{i}$. Because the analytical model assumes an infinitely large magnet array, weighting functions $\Delta(\vec{p})$ are introduced to smoothly switch the coils near the edge of the magnet array in such way that the analytical model is valid for the active coil set. The resulting expression for the currents in the set of active coils is given by [8]

$$\vec{i} = \Gamma^{-}(\vec{p})\vec{w} = \Delta(\vec{p})\Gamma(\vec{p})^{\bullet}\left(\Gamma(\vec{p})\Delta(\vec{p})\Gamma(\vec{p})^{\bullet}\right)^{-1}\vec{w}. \quad (51)$$

The switching of coils is illustrated in Fig. 26. In the bottom-left part of Fig. 26, the planar actuator with 24 active coils is shown. The active coils are dark gray, the coils which are switched off are light gray. The weighting functions do not penalize any coil. When the translator moves in the x-direction, the active coils in the left column will be smoothly switched off. After they are switched off, the adjacent coils in the outer right column will be smoothly switched on (not shown). At the transition, only 18 coils are active (bottom-right part of Fig. 26). When the translator moves in the y-direction only 20 coils are active at the transition between two different sets of coils (top-left part of Fig. 26). In the worst case situation (top-right part of Fig. 26), 9 coils are penalized by the weighting function and are switched off. As a result the planar actuator has 28 different sets of active coils. The 28 sets, in which the mass centre point of the magnet array can be located, are illustrated in Fig. 27.

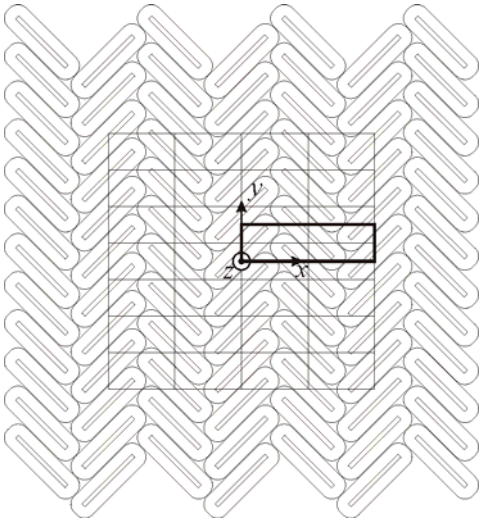

Fig. 27. Sets in which the mass centre point of the magnet array can be located.

The force and torque ripples in the commutated planar actuator have been predicted with the harmonic model. The planar actuator has been simulated in dark rectangular area shown in Fig. 27. The wrench set point was

$$\vec{w} = \begin{bmatrix} 15\text{ N} & 15\text{ N} & 15\text{ N} & 0\text{ Nm} & 0\text{ Nm} & 0\text{ Nm} \end{bmatrix}^{\bullet}. \quad (52)$$

Figs. 28 and 29 show the simulated and measured wrench on the translator of the planar actuator. The measurements show a sufficient decoupling between the force and the torque. The measured ripples are larger than predicted, but the rms force

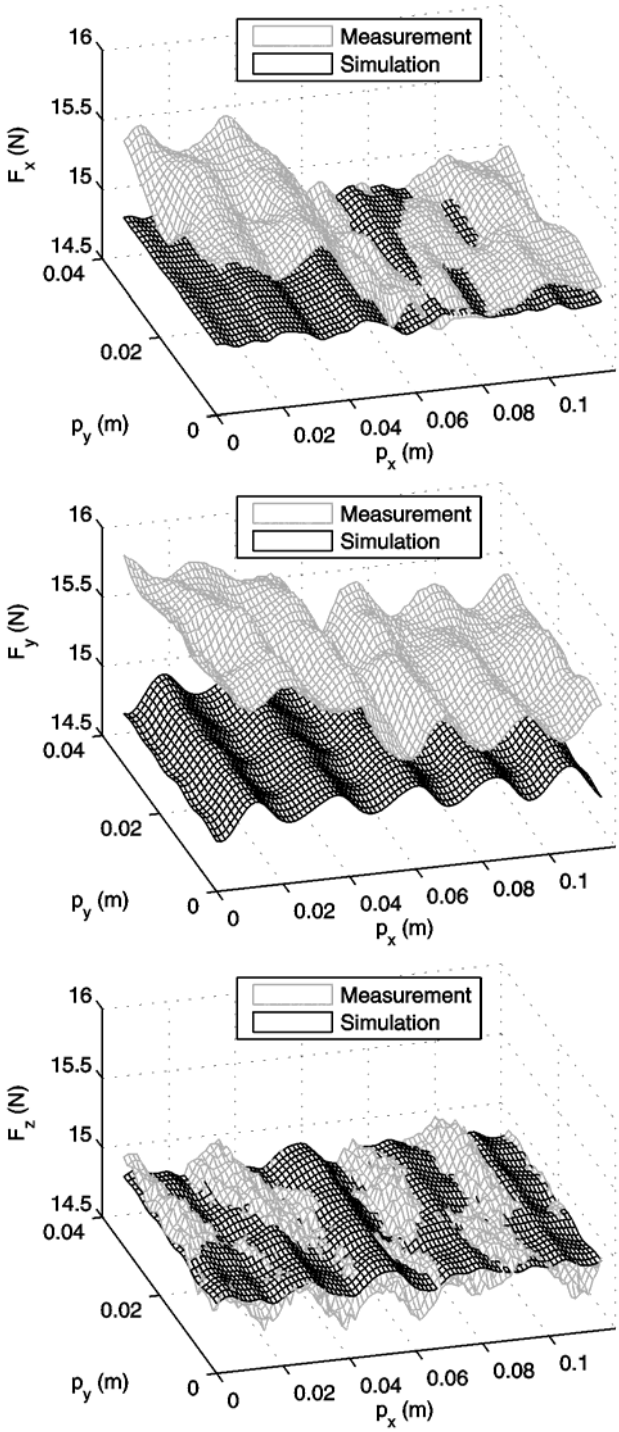

Fig. 28. Simulated and measured force on the translator of the planar actuator.

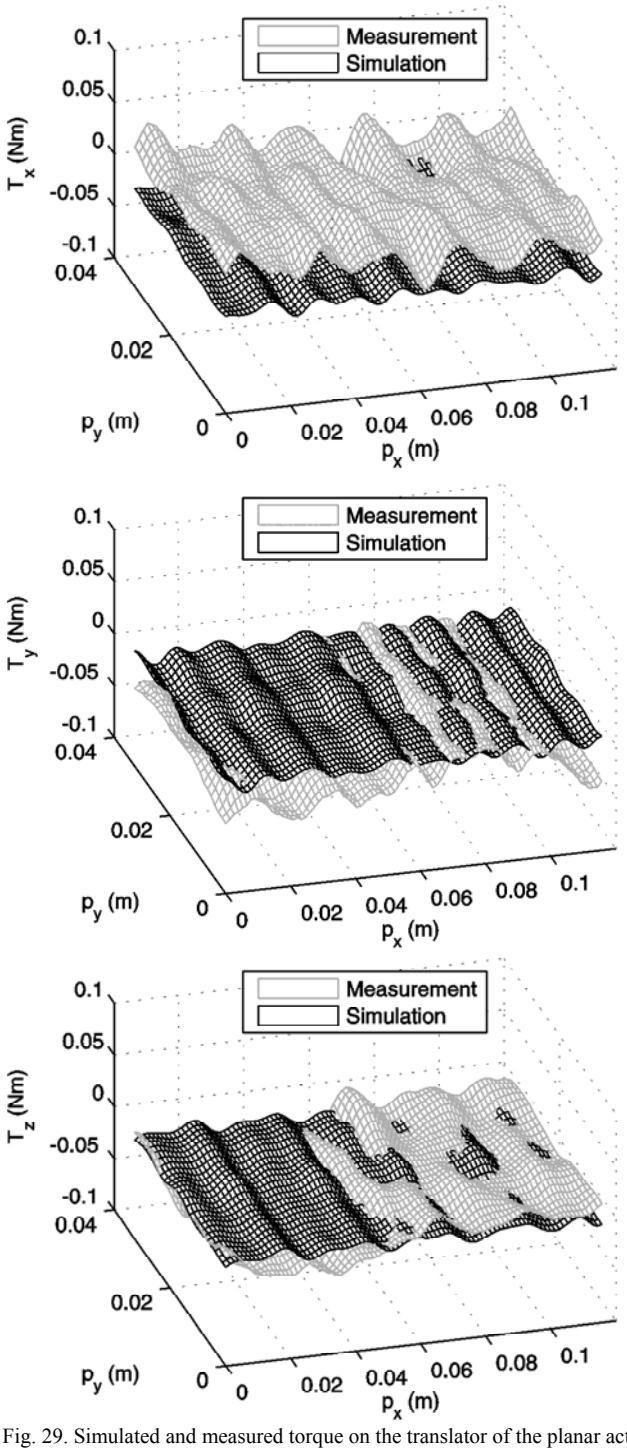

Fig. 29. Simulated and measured torque on the translator of the planar actuator.

ripples are less than 1.5% and the rms torque ripples are less than 15 mNm. The presented planar actuator has been fully designed and verified with the semi-analytical models discussed in the paper. A photo of the realized planar actuator and a part of the measurement system is shown in Fig. 30. The position of the planar actuator is measured contactlessly with inductive sensors with a range of 2 mm with respect to a measurement frame. This measurement frame is mounted on a conventional *xy*-positioning system with linear actuators. This external system follows the same trajectory as the planar actuator. However, there is no contact between both systems and the controllers of both systems are independent.

The tracking error of the planar actuator has been determined with six SISO quasi-PID controllers with mass and inertia feed-forward and with a bandwidth of 35 Hz. No MIMO

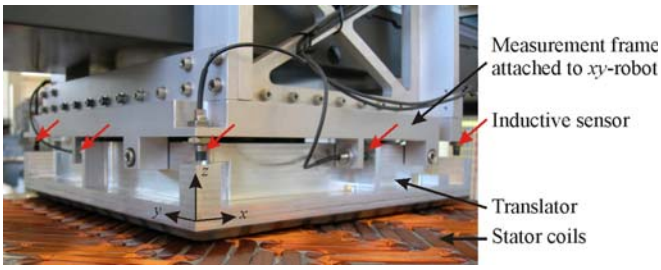

Fig. 30. Photo of the realized planar actuator and part of the measurement setup.

controller has been implemented because the wrench is sufficiently linearized and decoupled as shown in Figs. 27 and 28. When the translator is levitated 1.5 mm above the stator coils, the tracking error of the planar actuator is 30 µm and 100 µrad at full speed (1.4 m/s) and full acceleration (14 m/s^2).

At standstill operation the rms tracking error is less than 0.4 µm and 4 µrad (rms-tracking error: 0.1 µm and 1 µrad) [5]. The tracking error is limited by this measurement system and will be replaced by laser-interferometers in the near future. Current investigations are focused on the design of a new planar actuator with an accuracy in the nanometer range.

IX. Conclusions

Two (semi-)analytical modeling methods for the analysis and design of high-precision actuators have been presented and illustrated with practical examples. The models based on surface charges are very suitable to obtain fast and accurate three-dimensional magnetic flux density solutions of coreless magnet assemblies. The methods allow to calculate the forces between magnet assemblies and inside magnet assemblies. The surface charge method is very suitable for design and optimization of a gravity compensator. Furthermore, a harmonic model is presented with which both moving-magnet as well as moving-coil planar actuators can be designed. The harmonic model can be simply reduced to a fully analytical model which can be applied in the commutation algorithm of the planar actuator. The good performance of the realized planar actuator elucidates the capabilities of the presented (semi-)analytical models.

X. References

[1] Kim, W.J., Trumper, D.L., Lang, J.H., "Modeling and vector control of a planar magnetic levitator", *IEEE Trans. Ind. Applicat.*, vol. 34, no. 6, pp. 1254-1262, 1998.

[2] Hazelton, A.J., Binnard, M.B., Gery, J.M., "Electric motors and positioning devices having moving magnet arrays and six degrees of freedom", US Patent 6,208,045, 2001.

[3] Korenaga, N., "Alignment apparatus and exposure apparatus using the same", US Patent 7,705,198, 2006.

[4] Compter, J.C., Frissen, P.C.M., van Eijk, J., "Displacement device", Patent WO 2006/075,198, 2006.

[5] Jansen, J.W., van Lierop, C.M.M., Lomonova, E.A., Vandenput, A.J.A., "Ironless magnetically levitated planar actuator", *Journal of Applied Physics*, vol. 103, no. 7, 2008.

[6] de Boeij, J., Lomonova, E.A., Duarte, J., "Contactless planar actuator with manipulator: a motion system without cables and physical contact between the mover and the fixed world", *Industry Applications Society Annual Meeting, 2008. IAS '08. IEEE*, pp. 1–8, 2008.

[7] Compter, J.C., "Electro-dynamic planar motor", *Precision Engineering, vol. 28*, pp. 171-180, 2004.

[8] Lierop, C.M.M. van, Jansen, J.W., Lomonova, E.A., Damen, A.A.H., Bosch, P.P.J. van den, Vandenput, A.J.A., "Commutation of a magnetically levitated planar actuator with moving-magnets", *IEEJ Transactions on Industry Applications*, *128*(12), 1333-1338, 2008.

[9] Mizuno, T., Tasaki, M., Kishita, D., Hirakawa, K., "Vibration isolation system combining zero-power magnetic suspension with springs", *Control Engineering Practice*, vol. 15, no. 2, pp. 187–196, Feb. 2007.

[10] Hoque, E., Tasaki, M., Ishino, Y., Suzuki, H., Mizuno, T., "An active micro vibration isolator with zero-power controlled magnetic suspension technology", *JSME Int. Journal series C*, vol. 49, no. 3, pp. 15–34, 2006.

[11] Nagaya, K., Ishikawa, M., "A noncontact permanent magnet levitation table with electromagnetic control and its vibration isolation method using direct disturbance cancellation combining optimal regulators", *IEEE Trans. Magn.*, vol. 31, no. 1, pp. 885–896, Jan. 1995.

[12] Robertson, W., Cazzolato, B., Zander, A., "A multipole array magnetic spring", IEEE Trans. Magn., vol. 41, no. 10, pp. 3826–3828, Oct. 2005.

[13] Choi, K., Cho, Y., Shinshi, T., Shimokohbe, A., "Stabilization of one degree-of-freedom control type levitation table with permanent magnet repulsive forces", *Mechatronics*, vol. 13, pp. 587–603, 2002.

[14] Akoun, G., Yonnet, J.P., "2-D analytical calculation of the forces exerted between two cuboidal magnets", *IEEE Trans. Magn.*, vol. 20, no. 5, pp. 1962–1964, Sep. 1984.

[15] Hague, B., *The principles of electromagnetism applied to electrical machines*. New York: Dover Publications, 1962.

[16] Janssen, J.L.G., Paulides, J.J.H., Encica, L., Lomonova, E.A., "Analytical modeling of permanent magnets on a soft magnetic support for a suspension system*", Int. Conf. on Electrical Machines and Systems*, pp. 3825-3830, 2008.

[17] Jansen, J.W., van Lierop, C.M.M., Lomonova, E.A., Vandenput, A.J.A., "Magnetically Levitated Planar Actuator With Moving Magnets", *IEEE Transactions on Industrial Applications*, volume 44, issue 4, pp 1108-1115, 2008.

[18] Furlani, E.P., *Permanent Magnet and Electromechanical Devices: materials,analysis and applications*, 6th ed. London: Academic Press, 2001.

[19] Bancel, F., "Magnetic nodes," Journal of Applied Physics, vol. 32, pp. 2155–2161, Jun. 1999.

[20] Allag, H., Yonnet, J.P., Fassenet, M., Latreche, M., "3D analytical calculation of interactions between perpendicularly magnetized magnets – application to any magnetization direction", *Sensor Letters*, 2009, in press.

[21] Janssen, J.L.G., Paulides, J.J.H., Lomonova, E.A., "Analytical calculation of interaction force between orthogonally magnetized permanent magnets", *Sensor Letters*, 2009, in press.

[22] Medeiros, L., Reyne, G., Meunier, G., "Comparison of global force calculations on permanent magnets", *IEEE Trans. Magn.*, vol. 34, no. 5, pp. 3560–3563, Sep. 1998.

[23] Janssen, J.L.G., Paulides, J.J.H., Lomonova, E.A., "Passive magnetic suspension limitations for gravity compensation", *Journal of System Design and Dynamics*, 2009, in press.

[24] Rovers, J.M.M., Jansen, J.W., Lomonova, E.A., Ronde, M.J.C., "Calculation of the static forces among the permanent magnets in a Halbach array", *IEEE Trans. Magn.*, in press, 2009.

[25] Jansen, J.W., Lierop, C.M.M. van, Lomonova, E.A., Vandenput, A.J.A., "Modeling of magnetically levitated planar actuators with moving magnets", *IEEE Trans. Magn.*, vol. 43, no. 1, pp. 15-25, Jan. 2007.

Authors name and affiliation

J.W. Jansen*, J.L.G. Janssen, J.M.M. Rovers, J.J.H. Paulides, E.A. Lomonova
Electromechanics and Power Electronics group
Department of Electrical Engineering
Eindhoven University of Technology
Den Dolech 2
5612 AZ Eindhoven, The Netherlands

*Corresponding author
j.w.jansen@tue.nl